First-principles insights into the ferroelectric, dielectric, and piezoelectric properties of polar $Pca2_1$ SbN

Shihao Wang,[1] Zunyi Deng,[2] Shuhan Li,[1] Peng Lv,[3] Jing Wang,[1] Xueyun Wang,[2] Gang Tang,[1,*] and Jiawang Hong[2,†]

[1]*Advanced Research Institute of Multidisciplinary Science, Beijing Institute of Technology, Beijing 100081, China*

[2]*School of Aerospace Engineering, Beijing Institute of Technology, Beijing 100081, China*

[3]*Key Laboratory for Special Functional Materials of Ministry of Education, and School of Materials Science and Engineering, Henan University, Kaifeng 475004, China*

(Received 20 July 2023; revised 18 October 2023; accepted 23 October 2023; published 28 November 2023)

Binary nitride semiconductors have important applications in the industrial and technological fields. In this work, based on the recently reported metastable $Pca2_1$ phase of SbN, we investigated its structural stability, ferroelectric, dielectric, and piezoelectric properties using first-principles calculations. Our results indicate that the metastable SbN can be stabilized with a small hydrostatic pressure. Furthermore, we theoretically confirmed the presence of ferroelectricity in SbN, driven by stereochemically active Sb^{3+} $5s^2$ lone pair electrons. The estimated polarization value is close to that of traditional $PbTiO_3$. Moreover, SbN exhibits anisotropic dielectric constants, particularly in the ionic contribution part, primarily arising from the distinct mode-effective charges along different directions. In addition, SbN also exhibits a large d_{33} piezoelectric response, which is approximately four times larger than that of wurtzite-type AlN. The large d_{33} value is originated from the enhanced sensitivity of the atomic coordinates to the external strain $\frac{du_3}{d\eta_3}$ and softening of the elastic constant C_{33}. Therefore, our study provides meaningful theoretical guidance for the future experimental synthesis of stable binary nitride semiconductors and their device applications.

DOI: 10.1103/PhysRevB.108.174110

I. INTRODUCTION

Nitride materials have become increasingly important in the 21st century due to their crucial applications in industrial and technological fields. They possess unique bonding characteristics that result in electronic structures ranging from metallic to semiconducting, making them highly versatile in a wide range of applications. These applications include solar cells [1], light-emitting diodes (LEDs) [2], photocatalysts [3], power electronics [4,5], superconductors [6,7], piezoelectric materials [8,9], and so on. In the past decade, there has been increased focus on developing new ternary nitride semiconductors, including $ZnSnN_2$, $ZnGeN_2$, $CaZn_2N_2$, Zn_2SbN_3, and Mg_3SbN [10–13]. More recently, $LaWN_3$, a nitride perovskite material with polar symmetry, was successfully synthesized through experiments, exhibiting a strong piezoelectric response of 40 pm/V [14–16]. Compared to the widely developed ternary nitrides, binary nitride semiconductors are currently mostly limited to Group III nitrides in the wurtzite structure, particularly GaN and AlN, as well as their alloys such as $Al_xGa_{1-x}N$, $In_xGa_{1-x}N$, $Sc_xAl_{1-x}N$. Although GaN and AlN are crucial materials for key components in fifth-generation (5G) telecommunication technology and fourth-generation (4G) wireless networks, their development still faces some challenges. For examples, GaN is currently limited by the lack of high-quality bulk substrates required for vertical devices as well as its lower thermal conductivity [5]. AlN exhibits a low piezoelectric response, with d_{33} values ranging from 4.50 to 6.40 pC/N [17]. Although the piezoelectric response can be improved by doping Sc in AlN, it is difficult to achieve a uniform distribution of Sc in AlN at high alloy content [18]. More importantly, undoped binary Group III-nitride materials usually lack ferroelectric properties. Therefore, it is highly desired for exploring new polar binary nitride semiconductors.

Recently, a new binary nitride, antimony nitride (SbN), has been synthesized as a transition phase. Based on experimental results by Andriy Zakutayev *et al.*, it was revealed through *in situ* x-ray diffraction monitoring that a transient Sb-N phase formed during the rapid thermal annealing process at 500 °C and lasting for 17 s [19]. The observed phase is related to their predicted ground-state structure of SbN, based on the kinetically limited minimization approach. In contrast to binary Group III-nitrides, the crystal structure of SbN is characterized by space group $Pca2_1$ (No. 29), which belongs to the C_{2v} point group, one of the ten polar point groups. It is suggested that SbN displays piezoelectric properties and may also exhibit ferroelectric properties. However, SbN is currently in a metastable phase, and its properties cannot be fully characterized through experimental means alone. Therefore, further theoretical research is required to investigate its structural stability, as well as the ferroelectric, dielectric, and piezoelectric properties of SbN.

In this work, we first examined the structural properties and stability of the polar phase SbN, then systematically investigated its ferroelectric, dielectric, and piezoelectric properties

*gtang@bit.edu.cn
†hongjw@bit.edu.cn

through first-principles calculations. Our calculations reveal the distorted coordination environment in SbN, along with the distinct atomic arrangement along the three crystallographic axes. Furthermore, the reported SbN phase can be effectively stabilized either at a temperature of 300 K or under a hydrostatic pressure of 1 GPa. Based on the pressure-stabilized structure, our results demonstrate a remarkable spontaneous polarization greater than 70 μC/cm² in SbN, driven by the presence of occupied $5s^2$ lone pair electrons in the low-valent Sb^{3+} state. Moreover, SbN exhibits anisotropic dielectric properties, with a particularly small ion dielectric constant of $\varepsilon_{\text{ion}}^{yy} = 1.31$ along the layered direction. Finally, our investigation reveals a significantly enhanced piezoelectric response in SbN, with a d_{33} value of 20.27 pC/N, surpassing that of wurtzite-type AlN (5.44 pC/N).

II. METHODS

All calculations were performed with the Vienna *Ab initio* Simulation Package (VASP) based on the density functional theory (DFT) and the projector augmented wave method [20]. The strongly constrained and appropriately normed (SCAN) functional was chosen for structural relaxations and total energy calculations [21]. The valence electronic configurations for the pseudopotentials are as follows: $5s^25p^3$ for Sb and $2s^22p^3$ for N. The plane-wave cut-off energy was set to 450 eV. The Γ-centered 4 × 4 ×5 *k*-point meshes were employed for sampling the Brillouin zone. The lattice parameters and atomic positions were fully relaxed until the energy difference is less than 10^{-8} eV, and the force on each atom is smaller than 10^{-3} eV/Å. The Heyd-Scuseria-Ernzerhof (HSE) hybrid functional was employed to calculate density of states (DOS) and band structure [22]. The spin-orbit coupling was not taken into account in this study owing to its negligible influence on the electronic band structure of SbN. The elastic stiffness tensors were calculated using the strain-stress relationship with finite differences implemented in the VASP code. The Voigt-Reuss-Hill approximation [23–25] was used to estimate the bulk modulus, shear modulus, Young's modulus, and Poisson's ratio. The dielectric tensors and piezoelectric stress tensors were obtained using the density functional perturbation theory method [26,27]. Chemical bonding analysis within the framework of the crystal orbital Hamilton population (COHP) was performed using LOBSTER [28,29]. The phonon dispersion was calculated using the PHONOPY code with a 2 × 2 × 2 supercell based on the frozen-phonon method [30]. The room-temperature phonon spectrum was obtained by considering anharmonic phonon–phonon interactions with the temperature-dependent effective potential code [31,32].

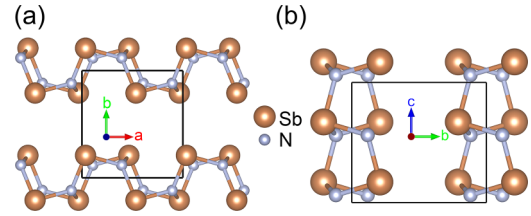

FIG. 1. Crystal structure of SbN along the (a) *ab* plane and (b) *bc* plane.

The *ab initio* molecular dynamics (AIMD) simulations were performed with a 3 × 3 × 3 supercell at an energy cutoff of 500 eV using the SCAN functional. The AIMD simulations were carried out in the canonical (NVT) ensemble at 300 K. The total simulation time was 6 ps with a time step of 3 fs. The structures were visualized using VESTA software [33]. The Bilbao Crystallographic Server was used for group theory analyses [34,35].

III. RESULTS AND DISCUSSION

A. Structure properties and stability

According to previous studies [19], the ground-state structure of SbN belongs to the noncentrosymmetric orthorhombic phase with a $Pca2_1$ (No. 29) space group, as shown in Fig. 1. It can be seen that SbN exhibits layered features along the *b* axis, with armchairlike chains along the *a* axis and zigzaglike chains along the *c* axis, resembling the typical black phosphorus. Each Sb (N) atom is surrounded by three nearest neighbor N (Sb) atoms at nonequidistant distances (2.06–2.09 Å). This distinct atomic arrangement along the three crystallographic axes results in highly anisotropic properties. The lattice parameters of SbN optimized using SCAN functionals are $a = 5.465$ Å, $b = 5.852$ Å, $c = 5.100$ Å, which shows the best consistency with previous reports (see Table I and Table S1 in the Supplemental Material [36]). The average Sb-N bond lengths are 2.068 Å and the average Sb-N-Sb bond angles are 111.9 degrees.

To understand the reasons behind the existence of three inequivalent Sb-N bonds, we investigated the expression of Sb $5s^2$ lone pair electrons. These $5s^2$ lone pair electrons have garnered significant interest in three-dimensional tin halide perovskites [37–39] and low-dimensional emissive metal halides [40]. Figure 2 illustrates the electron localization function (ELF) and the COHP. From Fig. 2(a), it can clearly be seen that the high values of the isosurface and the asymmetric spherical electron localization around the Sb atom are directly linked to its $5s^2$ lone pair electrons [41]. In the

TABLE I. The optimized structural parameters of SbN at 0 GPa (denoted as SbN@0) and 1 GPa (denoted as SbN@1), including lattice constants $a/b/c$, volume V, average Sb-N bond length d and average Sb-N-Sb bond angle θ. For comparison, the literature results are also provided.

	a (Å)	b (Å)	c (Å)	V (Å^3)	$d_{Sb\text{-}N}$ (Å)	$\theta_{\text{Sb-N-Sb}}$ (deg)
SbN@0	5.465	5.852	5.100	163.12	2.068	111.9
SbN@1	5.369	5.678	5.042	153.69	2.068	111.3
SbN (Ref.33)	5.4387	5.8249	5.0854	–	–	–

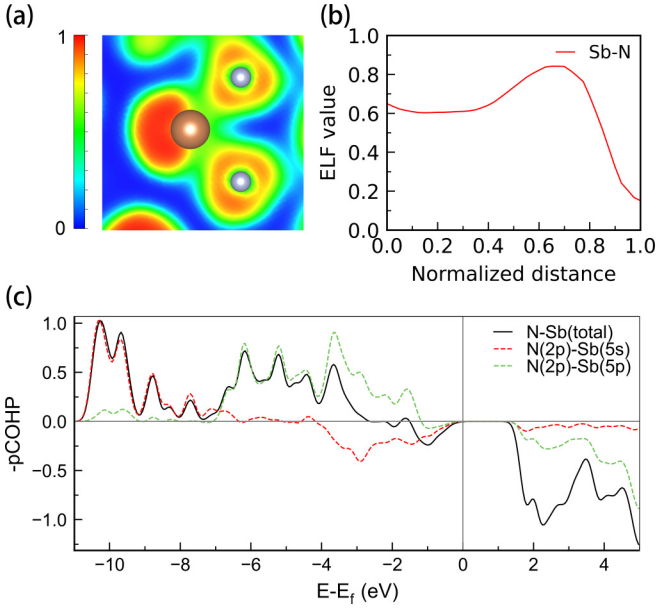

FIG. 2. (a) 2D schematic diagram of the electron localization function (ELF) for SbN@0, the isosurface level is 1.03 e/bohr^3. (b)1D profile of ELF value for SbN. (c) crystal orbital Hamilton population (COHP) of Sb-N bonds.

nonnuclear interaction region [as depicted in Fig. 2(b)], the presence of maximum values (> 0.8) of ELF signifies the formation of strong covalent bonds between the Sb and N atoms [42]. By combing the projected density of states (PDOS) (see Fig. S1 in the Supplemental Material [36]) and Fig. 2(c), it is evident that the Sb 5*s* states exhibit a strong hybridization with filled N 2*p* states in the valence band, resulting in the formation of bonding and antibonding states positioned at the lower and upper valence band, respectively. The latter is further stabilized by mixing with unoccupied Sb 5*p* states, giving rise to a high-energy occupied antibonding "midgap" state located above the N 2*p* states within the valence band [43]. Meanwhile, the presence of lone pair electrons also raises the valence band maximum. Consequently, SbN exhibits a relatively small band gap of 2.19 eV, which is significantly lower compared to AlN (6.2 eV) and GaN (3.4 eV) [44,45]. The occurrence of s-state feature in SbN is similar to the stereochemically active lone pair effects observed in other semiconductor materials such as SnS and PbO [46,47]. This is also consistent with the revised lone pair model proposed by Walsh *et al.* [48]. Based on our analysis, it is suggested that the energy difference between the Sb 5*s* states and N 2*p* states is relatively small, enabling the formation of stereochemically active lone pair electrons. The stereochemically activity of the Sb $5s^2$ lone pairs is responsible for the distorted coordination environment in SbN.

Considering the experimental synthesis of a metastable Sb-N phase appearing at 500 °C and lasting for 17 s [19], we first evaluated the thermodynamic stability of $Pca2_1$ phase SbN by calculating the energy above the convex hull (E_{hull}) relative to decomposition products. The E_{hull} value of SbN is 0.172 eV/atom, aligning well with the data reported by the Materials Project (0.17 eV/atom) [49,50]. Although slightly exceeding the stringent threshold of 0.1 eV/atom, it remains below 0.2

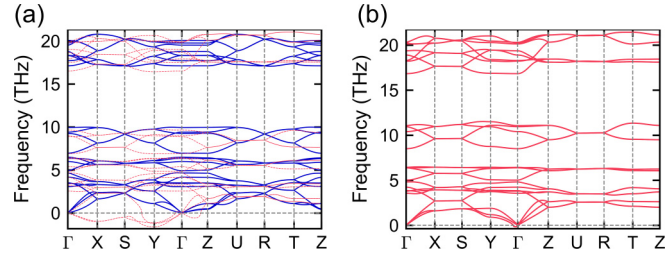

FIG. 3. Phonon dispersion curves of SbN. (a) At 0 GPa, with the red line representing 0 K and the blue line representing 300 K. (b) At 1 GPa and 0 K.

eV/atom, generally considered an acceptable range and also used as a criterion in relevant literature [51,52]. Moreover, recent studies [52,53] on metastable nitride semiconductors have demonstrated the efficacy of nonequilibrium synthesis mechanisms for stabilizing thermodynamically metastable phases. Molecular dynamics simulations and Helmholtz free energy calculations further confirm the thermodynamic stability of the $Pca2_1$ structure at finite temperatures (see Fig. S2 and S3 in the Supplemental Material [36]).

Next, we further investigated the lattice dynamical stability of $Pca2_1$ phase SbN. As shown in Fig. 3(a), the presence of imaginary frequencies in the phonon spectrum, particularly at the X point (0.5 0 0) and Y points (0 0.5 0), suggests that the $Pca2_1$ structure is dynamically unstable at 0 K. To stabilize these unstable modes, we displaced the atoms based on the force constant eigenvectors and generated several subgroup structures. Each of the obtained subgroup structures was then fully relaxed. After comparing the total energies of all the subgroup structures, we found that the *Pc* structure (see Fig. S4 [36]), obtained by simultaneously freezing the unstable phonon modes at the X and Y points, exhibits the lowest average energy per atom. Unfortunately, the existence of imaginary frequencies in the phonon spectra of *Pc* structure indicates that it was still dynamically unstable (see Fig. S5 [36]). Therefore, we further performed room temperature phonon spectrum calculation. The complete elimination of imaginary frequencies in the curves (see the blue line in Fig. 3) indicates the stability of SbN at 300 K. Additionally, we also applied a hydrostatic pressure strategy to successfully stabilize the unstable phonon modes in the original $Pca2_1$ structure at 0 K. After applying a hydrostatic pressure of 1 GPa to the $Pca2_1$ structure, the phonon spectra of pressurized structure (see Table I) only exhibit the negligible imaginary frequencies near the Γ point, indicating its dynamic stability at 0 K [see Fig. 3(b)]. In the following discussion, we will mainly focus on the various properties of SbN structure at 1 GPa.

B. Ferroelectric properties

First, we identified the high-symmetry nonpolar crystal structure of SbN utilizing the PSEUDO tool from the Bilbao Crystallographic Server [54]. Starting from the low-symmetry polar structure of SbN (space group $Pca2_1$), there are four centrosymmetric structures: *Pcca*, *Pbcm*, *Pbcn,* and *Pbca*. Among these structures, the *Pbcm* phase exhibits the smallest atomic displacement relative to the ferroelectric $Pca2_1$

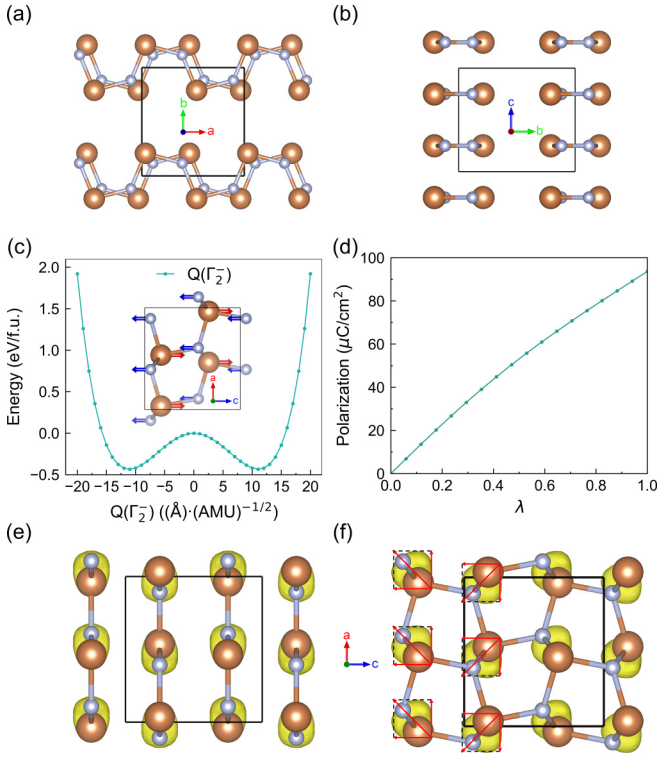

FIG. 4. Crystal structure of SbN in *Pbcm* phase (nonpolar) along the (a) *ab* plane and (b) *bc* plane. (c) The Kohn-Sham energy plotted as a function of Γ_2^-. The inset shows a schematic representation of the atomic displacement eigenvectors for the Γ_2^- mode. (d) The polarization as a function of normalized displacement λ, with the centrosymmetric structure at $\lambda = 0$ and the polar structure at $\lambda = 1$. The ELF of ferroelectric (e) and paraelectric (f) phases of SbN@1. The isosurface level is set to 0.95 e/bohr^3.

phase, as shown in Figs. 4(a) and 4(b). According to group theoretical analysis [55], there is only one phonon mode that transforms according to the irreducible representation Γ_2^-, which connects the prototypic *Pbcm* phase to the ferroelectric $Pca2_1$ phase. By examining the Γ_2^- mode, it is revealed that the dipole moment is induced by the displacement of Sb cations and N anions in opposite directions along the *c* axis, as shown in Fig. 4(c). The computed double-well potential [see Fig. 4(c)] confirms the relative stability of the ferroelectric $Pca2_1$ phase over the nonpolar *Pbcm* phase. The ferroelectric switching barrier of the $Pca2_1$ phase SbN@1 is calculated to be 0.43 eV/f.u., similar to that of $BiFeO_3$ (0.43 eV/f.u.), and lower than that of β-$CuGaO_2$ (0.90 eV/f.u.) [56]. This indicates that ferroelectric switching is possible in SbN@1.

The calculated spontaneous polarization values utilizing the Berry phase approach based on the modern theory of polarization [57], by interpolating between the nonpolar *Pbcm* phase ($\lambda = 0$) and the ferroelectric $Pca2_1$ phase ($\lambda = 1$), are shown in Fig. 4(d). The total polarization value for SbN@1 is determined to be 93.68 μC/cm^2 along the [0 0 1] direction. To consider the influence of the functional on the stereochemical expression of the Sb $5s^2$ lone pair, we also performed hybrid functional (HSE06) [22] calculations to optimize the structure and calculate the ferroelectric polarization in SbN. The calculated polarization value in SbN is 95.81 μC/cm^2. Therefore, the choice of functional does not severely impact the result. In addition, we also estimated the polarization value (76.61 μC/cm^2) of SbN@1 by multiplying the Born effective charges (BECs, see Table S2 [36]) by their atomic displacements relative to the *Pbcm* phase. This is smaller than the value obtained from the Berry phase approach, indicating a substantial electronic charge redistribution [58]. Such significant discrepancies between the two methods have also been observed in previous studies on ferroelectric materials $CsGeCl_3$ [58] and $SrBiNbSe_5$ [59]. The calculated polarization value in SbN@1 is comparable to well-known ferroelectrics: such as $LiNbO_3$ (~71 μC/cm^2) [60,61], $PbTiO_3$ (~90 μC/cm^2) [16,62] and LaN (~60 μC/cm^2) [63]. However, the polarization value of SbN@1 is slightly smaller compared to III-V semiconductor based ferroelectrics (i.e., $P_{Al_{0.73}Sc_{0.27}N} = 110\,\mu C/cm^2$ [64] and $P_{Al_{0.94}B_{0.06}N} = 130\,\mu C/cm^2$ [65]). Since the Born effective charges of Sb^{3+} (3.32 e) and N^{3-} (−3.32 e) along the *c* axis are only slightly larger than their normal charges (see Table S2 [36]), we attribute the large ferroelectric polarization in SbN@1 primarily to a large polar displacement arising from the lone pair electron effect.

TABLE II. The ionic (ε_{ion}) and electronic (ε_∞) contributions to the static dielectric constant (ε_{std}) for the SbN@0 and SbN@1. For comparison, the literature results are also provided.

	ε_{ion}^{xx}	ε_{ion}^{yy}	ε_{ion}^{zz}	$\varepsilon_{\infty}^{xx}$	$\varepsilon_{\infty}^{yy}$	$\varepsilon_{\infty}^{zz}$	ε_{std}^{xx}	ε_{std}^{yy}	ε_{std}^{zz}
SbN@0	3.77	0.99	5.28	7.28	5.64	7.87	11.05	6.63	13.15
SbN@1	3.98	1.31	5.86	7.85	6.56	8.49	11.83	7.88	14.34
AlN[a]	3.58	3.58	3.42	4.64	4.64	4.40	8.22	8.22	7.82
GaN[a]	3.81	3.81	3.73	5.87	5.87	5.69	9.68	9.68	9.42

[a]See Ref. [69].

Furthermore, we calculated the three-dimensional ELF of the ferroelectric and paraelectric phases of SbN@1 to investigate its ferroelectric origin, which may be potentially driven by the stereochemically active Sb $5s^2$ lone pair. As show in Fig. 4(e), in the paraelectric structure, the local dipoles from $5s^2$ lone pairs are fully compensated along the adjacent Sb-N chains. In contrast, the ELFs of the Sb^{3+} ion exhibit nonopposing distributions along the neighboring Sb-N chains, resulting in an uncompensated dipole along the *c* axis in the ferroelectric phase [Fig. 4(f)]. Therefore, these results confirms that the $5s^2$ lone pair of Sb^{3+} ion is a strong driving force of ferroelectricity. The driving mechanism is similar to the recently reported ferroelectric Bi_6O_9 [66].

C. Dielectric properties

Table II presents the static dielectric constants of SbN@0 and SbN@1. For SbN@1, the calculated dielectric constants are $\varepsilon_{std}^{xx} = 11.83$, $\varepsilon_{std}^{yy} = 7.88$ and $\varepsilon_{std}^{zz} = 14.34$. These values exhibit strong anisotropy related to the orthorhombic symmetry and distinct atomic arrangement along the three crystallographic axes. Notably, the dielectric constant along the *b* direction (ε_{std}^{yy}) is significantly smaller than that in the *ac* plane (ε_{std}^{xx} and ε_{std}^{zz}), indicating that SbN@1 possesses anisotropic screening capabilities for charged impurities and defects [67]. Furthermore, it is worth mentioning that the electronic contribution to the dielectric constant (ε_∞) of SbN@1 is

TABLE III. Elastic constants and mechanical properties including bulk modulus (B), shear modulus (G), Young's modulus (E), and Poisson's ratio (υ) of SbN@0 and SbN@1. For comparison, the literature results are also provided.

	C_{ij} (GPa)									B_{VRH}	G_{VRH}	E	
	C_{11}	C_{22}	C_{33}	C_{44}	C_{55}	C_{66}	C_{12}	C_{13}	C_{23}	(GPa)	(GPa)	(GPa)	υ
SbN@0	50.6	19.3	87.5	4.0	49.4	1.5	0.9	−11.6	3.5	14.0	30.3	13.3	0.14
SbN@1	62.3	38.7	90.2	4.6	52.9	1.7	4.6	−7.5	7.3	21.5	36.4	14.9	0.22
AlN[a]	407.6	–	386.8	128.4	–	–	128.8	93.5	–	203	137.8	337.3	0.22
GaN[a]	334.6	–	385.7	93.8	–	–	113	76.3	–	176	110.4	274.1	0.24

[a]See Ref. [73].

larger than that of III-V nitride semiconductors AlN and GaN, which can be attributed to the smaller band gap of SbN@1 relative to AlN and GaN [68]. On the other hand, compared to AlN and GaN, the ionic contribution to the dielectric constant (ε_{ion}) of SbN@1 is markedly smaller along the b axis, but significantly larger along the c axis.

To understand the anisotropic ε_{ion} in SbN, we examined the contribution of individual phonon modes to ε_{ion}. The mode-dependent dielectric permittivity tensor [70,71] is given as

$$\varepsilon^{\text{ion}}_{\alpha\beta}(\omega_\lambda) = \frac{\bar{Z}^*_{\lambda\alpha}\bar{Z}^*_{\lambda\beta}}{V\varepsilon_0 m_0 \omega^2_\lambda}, \tag{1}$$

where V is the volume per unit cell, $m_0 = 1$ a.m.u., ε_0 is the permittivity of the free space, and $\bar{Z}^*_{\lambda\alpha}$ is the mode-effective charge along the α-Cartesian direction for the λth phonon mode, which can be calculated from the atomic Born effective charges as

$$\bar{Z}^*_{\lambda\alpha} = \sum_{i\gamma} Z^*_{i\alpha\gamma}(\sqrt{m_0/m_i}\, v_{\lambda i\gamma}), \tag{2}$$

in which Z^*_i is the Born effective charge tensor for atom i, m_i is its atomic mass and $v_{\lambda i\gamma}$ is the normalized component of phonon eigenvector for mode λ on atom i along the γ Cartesian direction. According to Eqs. (1) and (2), the magnitude of ε_{ion} is governed by the mode-effective charge, infrared (IR)-active optical phonon frequency, and the total number of vibrational modes.

Based on the structure symmetry and group-theoretical analysis, SbN possesses 21 optical modes, of which 15 ($\Gamma_{\text{IR}} = 5A_1 + 5B_1 + 5B_2$) are IR active. Figure 5 illustrates the relative contribution of each IR mode to the ionic dielectric response along the three principal axes for SbN@1. It can be seen that $\varepsilon^{xx}_{\text{ion}}$, $\varepsilon^{yy}_{\text{ion}}$, and $\varepsilon^{zz}_{\text{ion}}$ are primarily contributed by the IR mode at 16–19 THz, with a secondary dominant IR mode at 8–11 THz. These optical modes mainly correspond to the motions of N atom. In the case of $\varepsilon^{xx}_{\text{ion}}$, the IR mode at $\omega_\lambda = 18.29$ THz contributes the most to the ionic response. For $\varepsilon^{yy}_{\text{ion}}$, the most prominent mode has a frequency of 18.89 THz. Regarding $\varepsilon^{zz}_{\text{ion}}$, the dominant mode is located at 16.83 THz. According to Eq. (1), the magnitude of ω_λ partially explains why $\varepsilon^{yy}_{\text{ion}}$ is the smallest and $\varepsilon^{zz}_{\text{ion}}$ is the largest. However, it does not fully account for the observed strong anisotropy. Next, we further analyzed the mode-effective charges. It can be found that the mode-effective charges of the dominant IR modes in $\varepsilon^{xx}_{\text{ion}}$ (−1.608 e) and $\varepsilon^{zz}_{\text{ion}}$ (−1.756 e) are approximately twice as large as those of the dominant IR modes in $\varepsilon^{yy}_{\text{ion}}$ (−0.816 e). Therefore, the mode-effective charges are the key factors determining the pronounced anisotropy in ε_{ion} observed in SbN@1.

D. Mechanical properties

Based on the orthorhombic symmetry of SbN, nine independent elastic constants were obtained, as shown in Table III. These constants fulfill the criteria for mechanical stability [72]. C_{11}, C_{22}, and C_{33} measure the resistance to linear compression along the crystallographic a, b, and c directions. From Table III, the trend of the principal elastic constants in SbN@1 being $C_{33} > C_{11} > C_{22}$ can be well understood in light of the sequence of their three lattice constants ($c < a < b$). This implies that in terms of uniaxial strains, the crystal exhibits its highest compressibility when the applied stress is oriented along the b direction, and its lowest compressibility when the stress is applied along the c direction.

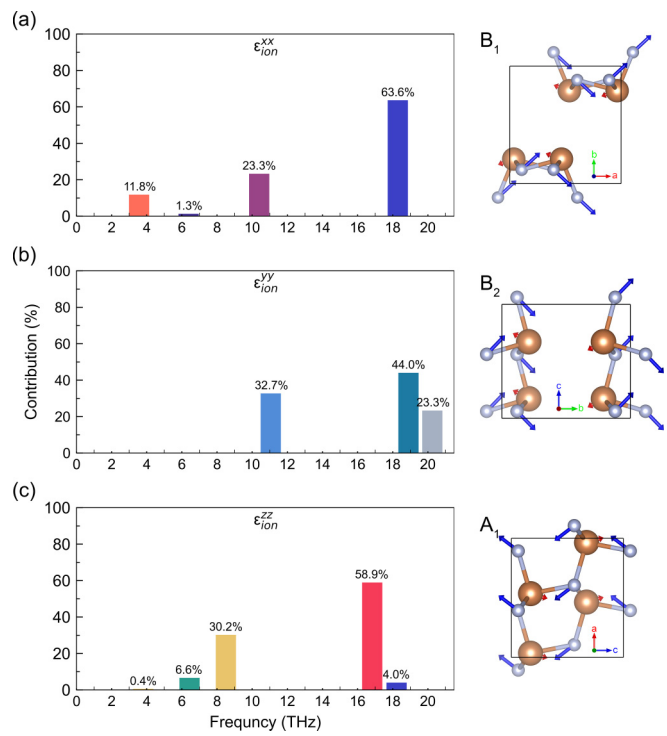

FIG. 5. Phonon mode contributions to the ionic part of the low-frequency dielectric tensor for SbN@1. The abscissa indicates the phonon frequencies. The second column pictures show atomic motions for the dominant mode in each direction: for $\varepsilon^{xx}_{\text{ion}}$, 18.29 THz; for $\varepsilon^{yy}_{\text{ion}}$, 18.89 THz; for $\varepsilon^{zz}_{\text{ion}}$, 16.83 THz.

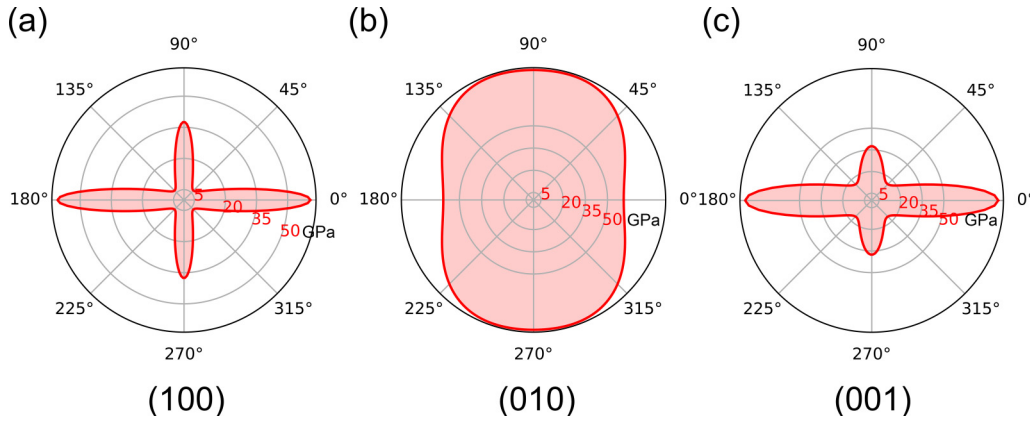

FIG. 6. Two-dimensional (2D) projection in polar coordinates in the (a) (001), (b) (010), and (c) (100) planes of the Young's modulus E of SbN@1.

This phenomenon can be attributed to the weak van der Waals interaction along the b direction, which greatly reduces the stiffness of the crystal. Meanwhile, the shear stiffness constants associated with the layered direction (i.e., $C_{44} = 4.6\,\text{GPa}$ and $C_{66} = 1.7\,\text{GPa}$) also exhibit notably smaller values compared to the nonlayered directions (i.e., $C_{55} = 52.9\,\text{GPa}$). This implies a very weak resistance to shear in the (100) and (001) planes.

Based on the obtained elastic stiffness matrix C_{ij}, we have also calculated the values of the bulk modulus (B), shear modulus (G), and Young's modulus (E), which are determined to be 21.5, 36.4, and 14.9 GPa, respectively. These values are significantly smaller compared to the corresponding values of III-V nitride semiconductors, such as AlN and GaN (see Table III), although the absolute ICOHP values for the Al-N and Ga-N bonds are 4.90 eV and smaller than that of the Sb-N bond at 5.27 eV. This suggests the difference in mechanical properties is more likely attributed to the stacking pattern of the crystal structure. The Pugh's ratio, which is the ratio between the bulk modulus, B, and the shear modulus, G (i.e., B/G), serves as an indicator of the ductility or brittleness of a material. According to the literature [74,75], the critical value separating ductile and brittle materials is 1.75. In the case of SbN@1, its Pugh's ratio is below 1.75, indicating that it exhibits a brittle nature. Finally, the directional Young's modulus $E(\theta)$ of SbN@1 are displayed in Fig. 6. The Young's modulus E projections on the (100) and (001) planes are highly anisotropic and reach the maximum value at 0 degree. This can be well understood from the layered nature of SbN@1 along the b direction.

E. Piezoelectric properties

In the case of SbN, the piezoelectric-stress have five independent elements, namely e_{31}, e_{32}, e_{33}, e_{24}, and e_{15}. Their calculated values for SbN@0 and SbN@1 are listed in Table IV. When the strain or shear strain is applied along the b direction, the piezoelectric stress constants exhibit negative values (i.e., $e_{32} = -0.075\,\text{C/m}^2$ and $e_{24} = -0.015\,\text{C/m}^2$). This can be attributed to the relatively weak van der Waals interaction along the layered direction [76]. All other piezoelectric stress constants, namely e_{31}, e_{33}, and e_{15}, exhibit positive values with the same sign. Among them, e_{33} exhibits the largest magnitude ($e_{33} = 1.695\,\text{C/m}^2$ for SbN@1). Furthermore, the e_{33} values of SbN@1 surpasses those of III-V nitride semiconductors, such as AlN ($1.498\ \text{C/m}^2$) and GaN ($0.73\ \text{C/m}^2$).

To have a deeper insight, we decompose e_{33} into two contributions:

$$e_{33} = e_{33}^{\text{clamp}} + \sum_{\kappa} e_{33}^{\text{int}}(\kappa) = e_{33}^{\text{clamp}} + \frac{c}{\Omega} \sum_{\beta,\kappa} Z_{3\beta}^{*}(\kappa) \frac{\mathrm{d}u_{\beta}(\kappa)}{\mathrm{d}\eta_3}. \tag{3}$$

The first term is the clamped-ion or homogeneous strain contribution to the piezoelectric tensor and it mainly arises

TABLE IV. The calculated stress and strain piezoelectric strain constants of SbN@0 and SbN@1. For comparison, the literature results are also provided.

	e_{ij} (C/m^2)					d_{ij} (pC/N)				
	e_{31}	e_{32}	e_{33}	e_{24}	e_{15}	d_{31}	d_{32}	d_{33}	d_{24}	d_{15}
SbN@0	0.507	−0.050	1.451	−0.005	0.073	14.43	−6.72	18.77	−1.35	1.47
SbN@1	0.493	−0.075	1.695	−0.015	0.097	10.88	−7.09	20.27	−3.35	1.84
AlN[a]	−0.685	–	1.498	–	−0.327	−2.76	–	5.44	–	−2.91
GaN	−0.49[b]	–	0.73[b]	–	−0.40[b]	−1.70[c]	–	3.40[c]	–	−3.10[c]

[a]See Ref. [77].
[b]See Ref. [78].
[c]See Ref. [79].

TABLE V. Born effective charges (Z^*_{33}) (|e|), $\frac{du_3}{d\eta_3}$, internal-strain $e^{\rm int}_{33}$ (C/m^2) for the atoms of each class, total internal-strain $e^{\rm int}_{33}$(total) (C/m^2), clamped-ion $e^{\rm clamp}_{33}$ (C/m^2), and total e_{33} (C/m^2).

Materials	atom	Z^*_{33}	$\frac{du_3}{d\eta_3}$	$e^{\rm int}_{33}$	$e^{\rm int}_{33}$(total)	$e^{\rm clamp}_{33}$	e_{33}
SbN	Sb	3.321	0.195	1.36	2.720	−0.880	1.840
	N	−3.321	−0.195	1.36			
w-AlN[a]	Al	2.680	0.093	0.94	1.880	−0.423	1.457
	N	−2.678	−0.093	0.94			
w-GaN[b]	–	–	–	–	1.5	−0.95	0.6

[a]See Ref. [9].
[b]See Ref. [80].

from the electronic contribution. The second term represents the contribution from the internal relaxation of ions. Here κ labels the atom within the primitive unit cell with volume Ω; Z^* is the Born effective charge, and $du_\beta(\kappa)$ is the fractional coordinate of the κth-atom along the β direction of the unit cell. Table V provides the individual atomic contributions to the internal strain ($e^{\rm int}_{33}$) term. The disparity in $e^{\rm int}_{33}$ values between SbN@1 and AlN can be attributed primarily to the variation in $\frac{du_3}{d\eta_3}$, which quantifies the response of the κth atom's internal coordinate along the c direction (u_3) to a macroscopic strain (η_3). Notably, SbN@1 exhibits twice the $\frac{du_3}{d\eta_3}$ value compared to AlN. Furthermore, the larger Born effective charge Z^*_{33} of SbN@1 also contributes to this discrepancy. Consequently, these factors together contribute to a higher e_{33} value in SbN@1 compared to AlN, even though SbN@1 possesses a larger primitive cell volume Ω and a more negative $e^{\rm clamp}_{33}$. On the other hand, the lower e_{33} value in GaN, in comparison to AlN and SbN@1, can be attributed to a combination of a smaller $e^{\rm int}_{33}$ and a more negative $e^{\rm clamp}_{33}$.

Based on the obtained piezoelectric stress constants e_{ik} and elastic stiffness constants C_{kj}, the corresponding piezoelectric strain constants d_{ij} can be determined as follows:

$$d_{ij} = \sum_{k=1}^{6} e_{ik} S_{kj}, \tag{4}$$

where S_{kj} is the elastic compliance matrix ($S_{kj} = (C_{kj})^{-1}$). All of the subscripts in the piezoelectric and elastic constants are given in Voigt notation. The values of d_{ij} for SbN@1 are presented in Table IV. It is evident that d_{31} (10.8 pC/N), and d_{33} (20.27 pC/N) exhibit favorable piezoelectric response. In particular, the calculated d_{33} value is approximately four times higher than that of AlN (5.44 pC/N) and even comparable to $Sc_xAl_{1-x}N$ (27.6 pC/N) [81,82].

To clarify the significant difference in d_{33} between SbN@1 and AlN, we further delved deeper into the reasons by analyzing Eq. (4). For SbN@1 with the $Pca2_1$ phase, the piezoelectric strain tensor component d_{33} can be expressed as $d_{33} = e_{31}S_{13} + e_{32}S_{23} + e_{33}S_{33}$. However, the combined contribution of the first two terms is relatively small, accounting for less than 5% of the total value of d_{33}. Therefore, the predominant factor influencing d_{33} is the interaction between e_{33} and S_{33}, which is approximately given by e_{33}/C_{33}. Previous studies [83,84] have estimated the value of d_{33} for AlN as e_{33}/C_{33}. In our calculation, the value of S_{33} for SbN is measured to be 0.0114 GPa^{-1}, which is approximately four times larger than that of AlN (0.0026 GPa^{-1}). Such large difference in d_{33} values can be attributed to the softening of the elastic constant C_{33} in SbN compared to AlN.

Finally, we evaluated the electromechanical coupling coefficient k_{ij} of SbN@1, which reflects the efficiency of energy conversion for piezoelectric materials. Interestingly, the value of k_{ij} for SbN@1 ($k_{33} = 0.53$) is larger compared those of typical inorganic piezoelectric materials such as ZnO ($k_{33} = 0.41$) and $BaTiO_3$ ($k_{33} = 0.35$) [85]. Therefore, SbN@1 shows promise for applications in piezoelectricity.

IV. CONCLUSION

In summary, we have systematically investigated the structural, ferroelectric, dielectric, and piezoelectric properties of SbN with $Pca2_1$ space group using the first-principles calculations. Our calculations indicate that the stereochemically active $5s^2$ lone pair electrons in the low-valent Sb^{3+} state lead to the distorted coordination environment in SbN. This is evidenced by the analyses of the PDOS, the COHP, and the ELF. After increasing the temperature to 300 K or applying a hydrostatic pressure of 1 GPa, the metastable SbN can be effectively stabilized. Furthermore, the pressure-stabilized SbN exhibits a spontaneous polarization greater than 70 μC/cm² along with a moderate switching barrier of 0.43 eV/f.u. between the ferroelectric and paraelectric state. The Sb^{3+} $5s^2$ lone-pair electrons play a crucial role in driving ferroelectricity by breaking the symmetry of the crystal and inducing the large polar displacements. Moreover, SbN exhibits anisotropic dielectric constants, particularly in the ionic contribution part ($\varepsilon^{xx}_{\rm ion} = 3.98$, $\varepsilon^{yy}_{\rm ion} = 1.31$ and $\varepsilon^{zz}_{\rm ion} = 5.86$), primarily arising from the distinct mode-effective charges along different directions ($\bar{Z}^*_{11} = -1.608\,$e, $\bar{Z}^*_{22} = -0.816\,$e, and $\bar{Z}^*_{33} = 1.756\,$e). Finally, the calculated d_{33} value in SbN (20.27 pC/N) is approximately four times higher than that of AlN (5.44 pC/N) and even comparable to $Sc_xAl_{1-x}N$ (27.6 pC/N). This enhancement can be attributed to the higher sensitivity of the atomic coordinates to the external strain $\frac{du_3}{d\eta_3}$ in SbN (±0.195) compared to AlN (±0.093), as well as the softening of the elastic constant C_{33} in SbN (90 GPa) compared to AlN (386.8 GPa). Our results suggest that SbN hold potential for applications in the fields of ferroelectricity and piezoelectricity, highlighting a potential new avenue for exploring polar binary nitride semiconductors.

ACKNOWLEDGMENTS

This work was supported by the National Key R&D Program of China (Grant No. 2021YFA1400300), the National Natural Science Foundation of China (Grant No. 12172047), and Beijing Natural Science Foundation (Grant No. Z190011). G.T. was supported by Beijing Institute of Technology Research Fund Program for Young Scholars (Grant No. XSQD-202222008). The calculations were carried out at National Supercomputer Center in Tianjin, and this research was supported by TianHe Qingsuo Project-special fund project.

[1] A. Zakutayev, Design of nitride semiconductors for solar energy conversion, J. Mater. Chem. A **4**, 6742 (2016).

[2] T.-Y. Seong, J. Han, H. Amano, and H. Morkoç, *III-Nitride Based Light Emitting Diodes and Applications* (Springer, New York, 2013).

[3] Y. Moriya, T. Takata, and K. Domen, Recent progress in the development of (oxy) nitride photocatalysts for water splitting under visible-light irradiation, Coord. Chem. Rev. **257**, 1957 (2013).

[4] T. Ueda, M. Ishida, T. Tanaka, and D. Ueda, GaN transistors on Si for switching and high-frequency applications, Jpn. J. Appl. Phys. **53**, 100214 (2014).

[5] J. Millan, P. Godignon, X. Perpiñà, A. Pérez-Tomás, and J. Rebollo, A survey of wide bandgap power semiconductor devices, IEEE Trans. Power Electron. **29**, 2155 (2013).

[6] V. Balbarin, R. Van Dover, and F. DiSalvo, The high temperature preparation and property measurements of CaTaN2: A ternary superconducting nitride, J. Phys. Chem. Solids **57**, 1919 (1996).

[7] X.-J. Chen, V. V. Struzhkin, Z. Wu, M. Somayazulu, J. Qian, S. Kung, A. N. Christensen, Y. Zhao, R. E. Cohen, and H.-k. Mao, Hard superconducting nitrides, Proc. Natl. Acad. Sci. USA **102**, 3198 (2005).

[8] D. Jena, R. Page, J. Casamento, P. Dang, J. Singhal, Z. Zhang, J. Wright, G. Khalsa, Y. Cho, and H. G. Xing, The new nitrides: Layered, ferroelectric, magnetic, metallic and superconducting nitrides to boost the GaN photonics and electronics eco-system, Jpn. J. Appl. Phys. **58**, SC0801 (2019).

[9] M. Noor-A-Alam, O. Z. Olszewski, and M. Nolan, Ferroelectricity and large piezoelectric response of AlN/ScN superlattice, ACS Appl. Mater. Interfaces **11**, 20482 (2019).

[10] A. Punya and W. R. Lambrecht, Band offsets between $ZnGeN_2$, GaN, ZnO, and $ZnSnN_2$ and their potential impact for solar cells, Phys. Rev. B **88**, 075302 (2013).

[11] Y. Hinuma, T. Hatakeyama, Y. Kumagai, L. A. Burton, H. Sato, Y. Muraba, S. Iimura, H. Hiramatsu, I. Tanaka, and H. Hosono, Discovery of earth-abundant nitride semiconductors by computational screening and high-pressure synthesis, Nat. Commun. **7**, 11962 (2016).

[12] E. Arca, J. D. Perkins, S. Lany, A. Mis, B.-R. Chen, P. Dippo, J. L. Partridge, W. Sun, A. Holder, and A. C. Tamboli, Zn_2SbN_3: Growth and characterization of a metastable photoactive semiconductor, Mater. Horiz. **6**, 1669 (2019).

[13] K. N. Heinselman, S. Lany, J. D. Perkins, K. R. Talley, and A. Zakutayev, Thin film synthesis of semiconductors in the Mg–Sb–N materials system, Chem. Mater. **31**, 8717 (2019).

[14] K. R. Talley, C. L. Perkins, D. R. Diercks, G. L. Brennecka, and A. Zakutayev, Synthesis of $LaWN_3$ nitride perovskite with polar symmetry, Science **374**, 1488 (2021).

[15] Y.-W. Fang, C. A. Fisher, A. Kuwabara, X.-W. Shen, T. Ogawa, H. Moriwake, R. Huang, and C.-G. Duan, Lattice dynamics and ferroelectric properties of the nitride perovskite $LaWN_3$, Phys. Rev. B **95**, 014111 (2017).

[16] C. Ederer and N. A. Spaldin, Effect of epitaxial strain on the spontaneous polarization of thin film ferroelectrics, Phys. Rev. Lett. **95**, 257601 (2005).

[17] X.-H. Zha, X. Ma, J.-T. Luo, and C. Fu, Enhanced piezoelectric response of AlN via alloying of transitional metals, and influence of type and distribution of transition metals, Nano Energy **111**, 108390 (2023).

[18] H. Momida, A. Teshigahara, and T. Oguchi, Strong enhancement of piezoelectric constants in $Sc_xAl_{1-x}N$: First-principles calculations, AIP Adv. **6**, 065006 (2016).

[19] B.-R. Chen, S. Lany, L. L. Kelly, E. Arca, Y. Iguchi, J. D. Perkins, H. Yanagi, M. F. Toney, L. T. Schelhas, and A. Zakutayev, Antimony nitride discovered by theoretical structure prediction, rapid thermal annealing, and *in situ* x-ray diffraction, Cell Rep. Phys. Sci. **3**, 100980 (2022).

[20] G. Kresse and D. Joubert, From ultrasoft pseudopotentials to the projector augmented-wave method, Phys. Rev. B **59**, 1758 (1999).

[21] J. Sun, A. Ruzsinszky, and J. P. Perdew, Strongly constrained and appropriately normed semilocal density functional, Phys. Rev. Lett. **115**, 036402 (2015).

[22] J. Heyd, G. E. Scuseria, and M. Ernzerhof, Hybrid functionals based on a screened Coulomb potential, J. Chem. Phys. **118**, 8207 (2003).

[23] R. Hill, The elastic behaviour of a crystalline aggregate, Proc. Phys. Soc. London, Sect. A **65**, 349 (1952).

[24] W. Voigt, Lehrbuch der kristallphysik:(mit ausschluss der kristalloptik) (BG Teubner, 1910), Vol. 34.

[25] A. Reuß, Berechnung der fließgrenze von mischkristallen auf grund der plastizitätsbedingung für einkristalle, ZAMM-J. Appl. Math. Mechanics/Z. Ange. Math. Mechan. **9**, 49 (1929).

[26] S. Baroni, P. Giannozzi, and A. Testa, Green's function approach to linear response in solids, Phys. Rev. Lett. **58**, 1861 (1987).

[27] P. Giannozzi, S. De Gironcoli, P. Pavone, and S. Baroni, *Ab initio* calculation of phonon dispersions in semiconductors, Phys. Rev. B **43**, 7231 (1991).

[28] R. Dronskowski and P. E. Blöchl, Crystal orbital Hamilton populations (COHP): Energy-resolved visualization of chemical bonding in solids based on density-functional calculations, J. Chem. Phys. **97**, 8617 (1993).

[29] V. L. Deringer, A. L. Tchougréeff, and R. Dronskowski, Crystal orbital Hamilton population (COHP) analysis as projected from plane-wave basis sets, J. Phys. Chem. A **115**, 5461 (2011).

[30] A. Togo and I. Tanaka, First principles phonon calculations in materials science, Scr. Mater. **108**, 1 (2015).

[31] O. Hellman and I. A. Abrikosov, Temperature-dependent effective third-order interatomic force constants from first principles, Phys. Rev. B **88**, 144301 (2013).

[32] O. Hellman, I. Abrikosov, and S. Simak, Lattice dynamics of anharmonic solids from first principles, Phys. Rev. B **84**, 180301 (2011).

[33] K. Momma and F. Izumi, VESTA: A three-dimensional visualization system for electronic and structural analysis, J. Appl. Crystallogr. **41**, 653 (2008).

[34] E. Kroumova, M. Aroyo, J. Perez-Mato, S. Ivantchev, J. Igartua, and H. Wondratschek, PSEUDO: A program for a pseudosymmetry search, J. Appl. Crystallogr. **34**, 783 (2001).

[35] J. Perez-Mato, D. Orobengoa, and M. Aroyo, Mode crystallography of distorted structures, Acta Crystallogr. Sect. A **66**, 558 (2010).

[36] See Supplemental Material at http://link.aps.org/supplemental/10.1103/PhysRevB.108.174110 for the structural parameters of SbN using different exchange-correlation functionals, the HSE06-calculated band structure and partial density of states (PDOS), the *ab initio* molecular dynamic (AIMD) simulations at 300 K, the Helmholtz free energy as a function of

temperature, the crystal structure and phonon dispersion curves for the *Pc* phase SbN, and the Born effective charges for the $Pca2_1$ phase SbN, which also includes Refs. [19,21,86–90].

[37] D. H. Fabini, G. Laurita, J. S. Bechtel, C. C. Stoumpos, H. A. Evans, A. G. Kontos, Y. S. Raptis, P. Falaras, A. Van der Ven, and M. G. Kanatzidis, Dynamic stereochemical activity of the Sn2+ lone pair in perovskite $CsSnBr_3$, J. Am. Chem. Soc. **138**, 11820 (2016).

[38] D. H. Fabini, R. Seshadri, and M. G. Kanatzidis, The underappreciated lone pair in halide perovskites underpins their unusual properties, MRS Bull. **45**, 467 (2020).

[39] M. W. Swift and J. L. Lyons, Lone-Pair Stereochemistry Induces Ferroelectric Distortion and the Rashba Effect in Inorganic Halide Perovskites, Chem. Mater. **35**, 9370 (2023).

[40] K. M. McCall, V. Morad, B. M. Benin, and M. V. Kovalenko, Efficient lone-pair-driven luminescence: Structure–property relationships in emissive $5s^2$ metal halides, ACS Mater. Lett. **2**, 1218 (2020).

[41] I. Maria, R. Arora, M. Dutta, S. Roychowdhury, U. V. Waghmare, and K. Biswas, Metavalent Bonding-Mediated Dual $6s^2$ Lone Pair Expression Leads to Intrinsic Lattice Shearing in n-Type $TlBiSe_2$, J. Am. Chem. Soc. **145**, 9292 (2023).

[42] K. Koumpouras and J. A. Larsson, Distinguishing between chemical bonding and physical binding using electron localization function (ELF), J. Phys.: Condens. Matter **32**, 315502 (2020).

[43] J. V. Handy, W. Zaheer, A. R. Rothfuss, C. R. McGranahan, G. Agbeworvi, J. L. Andrews, K. E. García-Pedraza, J. D. Ponis, J. R. Ayala, and Y. Ding, Lone but not alone: Precise positioning of lone pairs for the design of photocatalytic architectures, Chem. Mater. **34**, 1439 (2022).

[44] S. Loughin, R. French, W. Ching, Y. Xu, and G. Slack, Electronic structure of aluminum nitride: Theory and experiment, Appl. Phys. Lett. **63**, 1182 (1993).

[45] W. Lambrecht, B. Segall, J. Rife, W. Hunter, and D. Wickenden, UV reflectivity of GaN: Theory and experiment, Phys. Rev. B **51**, 13516 (1995).

[46] L. A. Jones, W. M. Linhart, N. Fleck, J. E. Swallow, P. A. Murgatroyd, H. Shiel, T. J. Featherstone, M. J. Smiles, P. K. Thakur, and T.-L. Lee, Sn $5s^2$ lone pairs and the electronic structure of tin sulphides: A photoreflectance, high-energy photoemission, and theoretical investigation, Phys. Rev. Mater. **4**, 074602 (2020).

[47] A. Walsh and G. W. Watson, The origin of the stereochemically active Pb (II) lone pair: DFT calculations on PbO and PbS, J. Solid State Chem. **178**, 1422 (2005).

[48] A. Walsh, D. J. Payne, R. G. Egdell, and G. W. Watson, Stereochemistry of post-transition metal oxides: Revision of the classical lone pair model, Chem. Soc. Rev. **40**, 4455 (2011).

[49] A. Jain, S. P. Ong, G. Hautier, W. Chen, W. D. Richards, S. Dacek, S. Cholia, D. Gunter, D. Skinner, G. Ceder, and K. A. Persson, Commentary: The Materials Project: A materials genome approach to accelerating materials innovation, APL Mater. **1**, 011002 (2013).

[50] A. Jain, G. Hautier, S. P. Ong, C. J. Moore, C. C. Fischer, K. A. Persson, and G. Ceder, Formation enthalpies by mixing GGA and GGA+ U calculations, Phys. Rev. B **84**, 045115 (2011).

[51] J. Döhn and A. Gross, Computational screening of oxide perovskites as insertion-type cathode material, ChemRxiv (2023).

[52] W. Sun, C. J. Bartel, E. Arca, S. R. Bauers, B. Matthews, B. Orvañanos, B.-R. Chen, M. F. Toney, L. T. Schelhas, and W. Tumas, A map of the inorganic ternary metal nitrides, Nat. Mater. **18**, 732 (2019).

[53] E. Arca, S. Lany, J. D. Perkins, C. Bartel, J. Mangum, W. Sun, A. Holder, G. Ceder, B. Gorman, and G. Teeter, Redox-mediated stabilization in zinc molybdenum nitrides, J. Am. Chem. Soc. **140**, 4293 (2018).

[54] C. Capillas, E. S. Tasci, G. de la Flor, D. Orobengoa, J. M. Perez-Mato, and M. I. Aroyo, A new computer tool at the Bilbao Crystallographic Server to detect and characterize pseudosymmetry, Z. Kristallogr. - Cryst. Mater. **226**, 186 (2011).

[55] D. Orobengoa, C. Capillas, M. I. Aroyo, and J. M. Perez-Mato, AMPLIMODES: Symmetry-mode analysis on the Bilbao Crystallographic Server, J. Appl. Crystallogr. **42**, 820 (2009).

[56] S. Song, D. Kim, H. M. Jang, B. C. Yeo, S. S. Han, C. S. Kim, and J. F. Scott, β-$CuGaO_2$ as a strong candidate material for efficient ferroelectric photovoltaics, Chem. Mater. **29**, 7596 (2017).

[57] R. King-Smith and D. Vanderbilt, Theory of polarization of crystalline solids, Phys. Rev. B **47**, 1651 (1993).

[58] Y. Zhang, E. Parsonnet, A. Fernandez, S. M. Griffin, H. Huyan, C.-K. Lin, T. Lei, J. Jin, E. S. Barnard, and A. Raja, Ferroelectricity in a semiconducting all-inorganic halide perovskite, Sci. Adv. **8**, eabj5881 (2022).

[59] R. Frey, B. F. Grosso, P. Fandré, B. Mächler, N. A. Spaldin, and A. M. Tehrani, Accelerated search for new ferroelectric materials, Phys. Rev. Res. **5**, 023122 (2023).

[60] S. Wemple, M. DiDomenico Jr., and I. Camlibel, Relationship between linear and quadratic electro-optic coefficients in $LiNbO_3$, $LiTaO_3$, and other oxygen-octahedra ferroelectrics based on direct measurement of spontaneous polarization, Appl. Phys. Lett. **12**, 209 (1968).

[61] A. Glass and M. Lines, Low-temperature behavior of spontaneous polarization in LiNb O 3 and LiTa O 3, Phys. Rev. B **13**, 180 (1976).

[62] Y. Zhang, J. Sun, J. P. Perdew, and X. Wu, Comparative first-principles studies of prototypical ferroelectric materials by LDA, GGA, and SCAN meta-GGA, Phys. Rev. B **96**, 035143 (2017).

[63] A. Rowberg, S. Mu, M. Swift, and C. Van de Walle, Structural, electronic, and polarization properties of YN and LaN, Phys. Rev. Mater. **5**, 094602 (2021).

[64] S. Fichtner, N. Wolff, F. Lofink, L. Kienle, and B. Wagner, AlScN: A III-V semiconductor based ferroelectric, J. Appl. Phys. **125**, 114103 (2019).

[65] S. Calderon, J. Hayden, S. M. Baksa, W. Tzou, S. Trolier-McKinstry, I. Dabo, J.-P. Maria, and E. C. Dickey, Atomic-scale polarization switching in wurtzite ferroelectrics, Science **380**, 1034 (2023).

[66] Q. Yang, J. Hu, Y.-W. Fang, Y. Jia, R. Yang, S. Deng, Y. Lu, O. Dieguez, L. Fan, and D. Zheng, Ferroelectricity in layered bismuth oxide down to 1 nanometer, Science **379**, 1218 (2023).

[67] R. E. Brandt, J. R. Poindexter, P. Gorai, R. C. Kurchin, R. L. Hoye, L. Nienhaus, M. W. Wilson, J. A. Polizzotti, R. Sereika, and R. Zaltauskas, Searching for "defect-tolerant" photovoltaic materials: Combined theoretical and experimental screening, Chem. Mater. **29**, 4667 (2017).

[68] A. Takahashi, Y. Kumagai, J. Miyamoto, Y. Mochizuki, and F. Oba, Machine learning models for predicting the dielectric

constants of oxides based on high-throughput first-principles calculations, Phys. Rev. Mater. **4**, 103801 (2020).

[69] C. Persson, R. Ahuja, A. F. da Silva, and B. Johansson, First-principle calculations of optical properties of wurtzite AlN and GaN, J. Cryst. Growth **231**, 407 (2001).

[70] W. Cochran, Crystal stability and the theory of ferroelectricity, Adv. Phys. **9**, 387 (1960).

[71] E. Cockayne and B. P. Burton, Phonons and static dielectric constant in $CaTiO_3$ from first principles, Phys. Rev. B **62**, 3735 (2000).

[72] F. Mouhat and F.-X. Coudert, Necessary and sufficient elastic stability conditions in various crystal systems, Phys. Rev. B **90**, 224104 (2014).

[73] M. Fatmi, B. Ghebouli, M. Ghebouli, and Z. Hieba, First-principles study of structural, elastic, electronic, lattice dynamic and optical properties of XN ($X =$ Ga, Al, and B) compounds under pressure, Phys. Scr. **83**, 065702 (2011).

[74] H. Fu, D. Li, F. Peng, T. Gao, and X. Cheng, *Ab initio* calculations of elastic constants and thermodynamic properties of NiAl under high pressures, Comput. Mater. Sci **44**, 774 (2008).

[75] Y. Yang, H. Lu, C. Yu, and J. Chen, First-principles calculations of mechanical properties of TiC and TiN, J. Alloys Compd. **485**, 542 (2009).

[76] Y. Qi and A. M. Rappe, Widespread negative longitudinal piezoelectric responses in ferroelectric crystals with layered structures, Phys. Rev. Lett. **126**, 217601 (2021).

[77] Z. Almaghbash, O. Arbouche, A. Dahani, A. Cherifi, M. Belabbas, and B. Djellouli, Significant improvement in the piezoelectric properties and electromechanical coupling factors of wurtzite AlN compound under high pressures, J. Comput. Electron. **20**, 2420 (2021).

[78] B. K. Sahoo, Effect of piezoelectric polarization on phonon group velocity in nitride wurtzites, J. Mater. Sci. **47**, 2624 (2012).

[79] I. Guy, E. Goldys, and S. Muensit, in *2000 International Semiconducting and Insulating Materials Conference. SIMC-XI (Cat. No. 00CH37046)* (IEEE, New York, 2000), p. 55.

[80] K. S. Suzuki and H. O. H. Okumura, First-principles study on piezoelectric constants in strained BN, AlN, and GaN, Jpn. J. Appl. Phys. **37**, L1421 (1998).

[81] M. Akiyama, T. Kamohara, K. Kano, A. Teshigahara, Y. Takeuchi, and N. Kawahara, Enhancement of piezoelectric response in scandium aluminum nitride alloy thin films prepared by dual reactive cosputtering, Adv. Mater. **21**, 593 (2009).

[82] M. Akiyama, K. Kano, and A. Teshigahara, Influence of growth temperature and scandium concentration on piezoelectric response of scandium aluminum nitride alloy thin films, Appl. Phys. Lett. **95**, 162107 (2009).

[83] F. Tasnádi, B. Alling, C. Höglund, G. Wingqvist, J. Birch, L. Hultman, and I. A. Abrikosov, Origin of the anomalous piezoelectric response in wurtzite $Sc_x Al_{1-x}N$ alloys, Phys. Rev. Lett. **104**, 137601 (2010).

[84] R. Matloub, M. Hadad, A. Mazzalai, N. Chidambaram, G. Moulard, C. Sandu, T. Metzger, and P. Muralt, Piezoelectric Al1− xScxN thin films: A semiconductor compatible solution for mechanical energy harvesting and sensors, Appl. Phys. Lett. **102**, 152903 (2013).

[85] X. Wu, D. Vanderbilt, and D. Hamann, Systematic treatment of displacements, strains, and electric fields in density-functional perturbation theory, Phys. Rev. B **72**, 035105 (2005).

[86] S. H. Vosko, L. Wilk, and M. Nusair, Accurate spin-dependent electron liquid correlation energies for local spin density calculations: A critical analysis, Can. J. Phys. **58**, 1200 (1980).

[87] J. P. Perdew, A. Ruzsinszky, G. I. Csonka, O. A. Vydrov, G. E. Scuseria, L. A. Constantin, X. Zhou, and K. Burke, Restoring the density-gradient expansion for exchange in solids and surfaces, Phys. Rev. Lett. **100**, 136406 (2008).

[88] J. P. Perdew, K. Burke, and M. Ernzerhof, Generalized gradient approximation made simple, Phys. Rev. Lett. **77**, 3865 (1996).

[89] S. Grimme, J. Antony, S. Ehrlich, and H. Krieg, A consistent and accurate ab initio parametrization of density functional dispersion correction (DFT-D) for the 94 elements H-Pu, J. Chem. Phys. **132**, 154104 (2010).

[90] H. Peng, Z.-H. Yang, J. P. Perdew, and J. Sun, Versatile van der Waals density functional based on a meta-generalized gradient approximation, Phys. Rev. X **6**, 041005 (2016).